Compact atom-interferometer gyroscope based on an expanding ball of atoms

S Riedl, G W Hoth, B Pelle, J Kitching and E A Donley

Time and Frequency Division, National Institute of Standards and Technology, Boulder, CO, USA

E-mail: elizabeth.donley@nist.gov

Abstract. We present a compact atom interferometer based on ^{87}Rb atoms that can simultaneously measure rotations and accelerations with a single expanding ball of atoms in a 300 cm^3 vacuum package.

1. Introduction

Inertial sensors based on phase shifts accumulated by matter waves in atom interferometers are a promising technology for high-performance inertial navigation. Acceleration and rotation measurements with these sensors have demonstrated sensitivities of 4.2×10^{-8} m/s^2/$\sqrt{\text{Hz}}$ in a cold-atom gravimeter [1], 80 μdeg/$\sqrt{\text{hr}}$ in a gyroscope based on thermal atomic beams [2, 3], and 400 μdeg/$\sqrt{\text{hr}}$ in a cold-atom gyroscope [4]. These instruments comfortably operate within the specifications for navigation-grade performance (5×10^{-5} m/s^2/$\sqrt{\text{Hz}}$ and 1×10^{-3} deg/$\sqrt{\text{hr}}$) [5]. However, atom interferometers that achieve this performance are many meters in scale. Our goal is to apply these methods in dramatically smaller systems and explore the trade-offs between performance and portability. Here we consider atoms confined in an active volume of 1 cm^3.

While high-performance atom interferometers are becoming more common in laboratory environments, there are only a few published demonstrations performed on moving vehicles [6-8], including an airborne accelerometer demonstration in a vibrationally noisy environment [6, 7]. While portable, these instruments were very complex, and the equipment to run them occupied several cubic meters. Atom-interferometer gyroscopes are even more complex given that they require counter-propagating atom sources with separate atom launch and detection systems. Simplifications to the approach of building atom-interferometer gyroscopes may eventually facilitate their use in portable applications.

Most atom-interferometer inertial sensors are based on stimulated Raman transitions [9], where
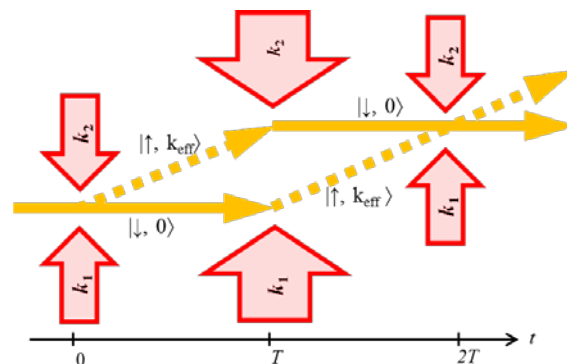
Figure 1. Mach-Zehnder type atom interferometer. The lines represent classical trajectories for the atoms, which undergo transitions between the internal states $|\uparrow\rangle$ (dashed) or $|\downarrow\rangle$ (solid lines). The red arrows represent the Raman pulses. (Colour online).

atoms are excited into superposition states with pairs of counterpropagating laser beams tuned into Raman resonance with the atomic hyperfine splitting. The absorption and stimulated emission of photon pairs imparts momentum to the atoms and simultaneously alters the internal hyperfine level [10]. Typically three Raman pulses are used (Red arrows in figure 1). The first $\pi/2$ pulse prepares each atom in a superposition state. The atomic wavepacket is split such that the part that has undergone a stimulated Raman transition also receives a momentum kick of $\hbar \vec{k}_{\text{eff}}$, where $\vec{k}_{\text{eff}} = (\vec{k}_1 - \vec{k}_2)$ is the effective wave vector for the two-photon Raman transition and $\hbar$ is the reduced Plank's constant. After the $\pi/2$ pulse, the phase of each state evolves independently for a period, T, and then a π pulse exchanges the atomic states. The atoms are again allowed to evolve for a period T. Finally, another $\pi/2$ pulse interferes the states and the combined acceleration- and rotation-induced phase shift is determined from a measurement of the final atomic hyperfine population. For atoms moving with an initial velocity $\vec{v}$, this phase shift is

$$\varphi_{\text{int}} = \varphi_{\text{acc}} + \varphi_{\text{rot}} = \vec{k}_{\text{eff}} \cdot \vec{a} T^2 + 2\vec{k}_{\text{eff}} \cdot (\vec{\Omega} \times \vec{v}) T^2, \tag{1}$$

where φ_{acc} and φ_{rot} are the acceleration- and rotation-induced phase shifts, $\vec{a}$ is the acceleration, and $\vec{\Omega}$ is the rotation rate. The rotation term can also be expressed in the Sagnac form as $\varphi_{\text{rot}} = \frac{2m}{\hbar} \vec{\Omega} \cdot \vec{A}$, which is proportional to the enclosed area $\vec{A}$ and the rotation rate, and where m is the atomic mass. The interferometer phase is sensitive to accelerations along the direction of the light propagation and rotations perpendicular to this direction (and perpendicular to $\vec{v}$).

The interferometer signal is extracted from the hyperfine population after the third pulse as

$$P(\uparrow) = 1 - P(\downarrow) = \frac{1}{2}(1 - C\cos(\varphi_{\text{int}} + \varphi_0)). \tag{2}$$

$P(\uparrow)$ $[P(\downarrow)]$ is the probability that the atom is in the upper [lower] hyperfine state at the interferometer output, φ_0 is a constant phase offset, and C is the interferometer fringe contrast.

The acceleration and rotation components of φ_{int} cannot typically be distinguished with a single measurement; they are typically extracted by use of two independent counterpropagating atom sources. Because the sign of φ_{rot} depends on the sign of $\vec{v}$, subtracting the $+v$ signal from the $-v$ signal uniquely determines $\vec{\Omega}$. In thermal atomic-beam gyroscopes, this is accomplished with two opposing atom source ovens [2]. For interferometer gyroscopes based on laser-cooled atoms, two separate magneto-optic traps (MOTs) collect and launch atoms in opposite directions [11, 12].

Our system is a cold-atom combination accelerometer/gyroscope based on a single expanding ball of laser-cooled atoms probed using spatially resolved detection of the atomic states. This approach is much simpler than the conventional designs for atom interferometer gyroscopes that require differential measurements from two atom sources. Our work extends the point source interferometry (PSI) technique originally demonstrated in a 10-m tower at Stanford [13] into a new regime for portable applications. Our vacuum system is 100× smaller in height, our atoms are 1000× warmer, and our interaction periods are 200× shorter than those reported in [13]. Our ultimate goal is to determine if such a compact system with a short interrogation period can be competitive in high-performance inertial navigation applications.

2. Experimental Approach

The PSI technique uses a single source of atoms with a broad range of velocities in combination with spatially resolved detection to separate acceleration- and rotation-induced phase shifts. Because the individual atom velocities are correlated with their final positions after the interferometer sequence, rotational phase shifts appear as spatial interference fringes in the atomic states across the atom ball, while the overall phase shift of the central fringe determines the acceleration.

The principles of the sensor are shown in figure 2. An ensemble of ^{87}Rb atoms is collected and cooled in a magneto-optical trap (MOT) and post-cooled with an optical molasses into a volume smaller than a millimeter in diameter. After a brief free fall that allows the Doppler-sensitive and insensitive transitions to be resolved [14] (not shown), the Raman pulses are applied by a pair of laser beams counter-propagating along $+\hat{z}$ and $-\hat{z}$.

Because of the correlation between the atoms' initial velocity and their final position, the final rotation-induced interferometer phase is a function of spatial location. With the $\vec{k}_{\text{eff}}$ along $+\hat{z}$ and for rotation about $\hat{y}$, atoms moving toward $+\hat{x}$ will produce a negative phase shift, while those moving along $-\hat{x}$ will have a positive phase shift. The phase shift will be linear in spatial position $\hat{x}$ at the end of the second interaction period. Similarly, rotation about $\hat{x}$ will cause a linearly varying phase along $\hat{y}$. The spatially-dependent phase is read out using absorption imaging of the cloud with a resonant laser propagating along $\hat{z}$. Under rotation, fringes in the atom population in the absorption image will be observed in the direction $\vec{k}_{\text{eff}} \times \vec{\Omega}$, and can be distinguished around any axis in the $\hat{x} - \hat{y}$ plane.

Physically, this phase shift arises because the expanding cloud contains many atom interferometer trajectories with different enclosed areas. The small size of the initial atom cloud and the radial expansion of the cloud during the interaction period create a correlation between the final atom position and the area enclosed by the atom trajectory. For example, atoms having an initial velocity perpendicular to the Raman beams will have a maximal enclosed area of $\left(\frac{\hbar k_{\text{eff}}}{m}\right) v_0 T^2$, while atoms having an initial velocity v_0 parallel to the Raman beams will have zero enclosed area, because the momentum imparted by the Raman beams is entirely along the direction of the initial velocity. In general, the enclosed area only depends on the projection of the final position of the atom in the $\hat{x} - \hat{y}$ plane perpendicular to $\vec{k}_{\text{eff}}$. Thus, for fixed interaction time, T, all atoms at the same $\hat{x} - \hat{y}$ position (independent of $\hat{z}$ position) undergo the same phase shift and complete the interferometer pulse sequence in the same superposition of hyperfine states.
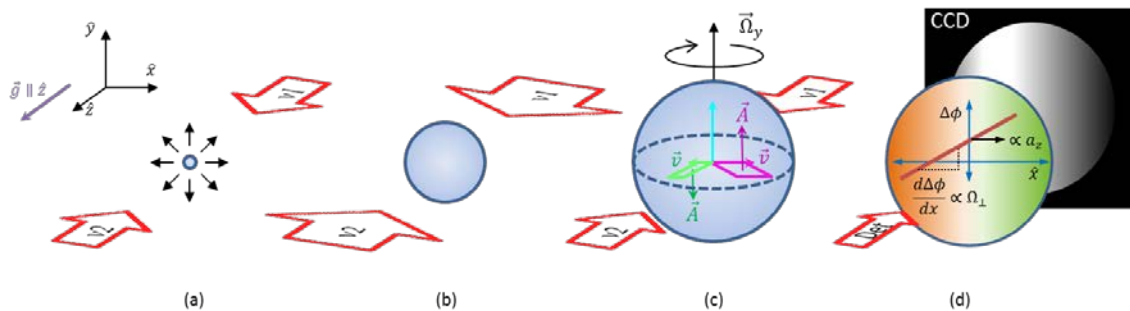
Figure 2. Atom interferometry with an expanding ball of atoms. (a) Initial expanding cloud. (b) Second Raman-Ramsey pulse applied mid-way through expansion. (c) After the full expansion, there is a phase gradient on the cloud. This occurs because the transverse velocity of each atom determines the area enclosed by the trajectory of that atom through the interferometer. This is illustrated here with two sample trajectories corresponding to different transverse velocities. (d) The interferometer phase gradient is imprinted in the atom populations and is read out by a detection beam. The phase gradient is perpendicular to both $\vec{k}_{\text{eff}}$ and $\vec{\Omega}$. The offset of the phase gradient from zero at the cloud's center depends on the acceleration component along $\hat{z}$. In this example as well as in the experiment, the Raman pulses are parallel to gravity. (Colour online).

3. Apparatus
A schematic diagram of the laser system and the physics package is shown in figure 3.

3.1. Vacuum System
The vacuum system is based on a 7.5 cm^3 uncoated spectrometer cell fused to a glass tee that is equipped with two Rb dispensers and sealed onto a 34 mm mini-conflat flange. The cell is mounted to a mini-conflat six-way cross opposite to a glass viewport. A 2 l/s ion pump and a non-evaporable getter pump are also mounted to the six-way cross. The volume of the entire vacuum system is ~300 cm^3. The system is currently not magnetically shielded.

3.2. Laser System

There are currently three distributed Bragg reflector (DBR) lasers used in the interferometer. One laser is used for the MOT cooling light and is locked by saturated absorption spectroscopy and shifted by an AOM to a detuning of two linewidths from the $F = 2 \rightarrow F' = 3$ cycling transition. This laser serves as a reference for the Raman lasers, whose frequency differences from the MOT laser are computer-controlled and set to different values as the lasers play various roles during the experiment [15].

The first of these two frequency-agile lasers is frequency locked to the MOT laser and serves both as the Raman beam for the $F = 2 \rightarrow F'$ transition and the resonant probe beam for detection. The second frequency-agile laser serves as the Raman beam for the $F = 1 \rightarrow F'$ transition, as a repump laser for laser cooling and detection of the $F = 1$ atoms after an interferometer cycle, and for optically pumping the atoms into the $F = 1$, $m_F = 0$ state at the start of each interferometer cycle. The two frequency-agile lasers are phase locked to each other with a frequency offset of 6.834 GHz with an optical phase-locked loop. We typically have about 70 % of the beat-note power in the coherent carrier, which is limited by the frequency modulation bandwidth of the DBR lasers. The difference frequency between the Raman lasers is chirped at a rate of $\vec{k}_{\mathrm{eff}} \cdot \vec{g} = 25.1$ kHz/ms to maintain Raman resonance for all three interferometer pulses. The frequencies of the Raman beams are typically detuned by 200 MHz from the $F' = 0$ resonance. The Raman beams are overlapped with orthogonal polarizations and fiber coupled to the apparatus with a PM fiber. The Raman beams are 7 mm in diameter ($1/e^2$). Typically 4 mW of $F = 1$ light and 10 mW of $F = 2$ light are used for the Raman pulses. The Raman beams go through the cell vertically and the $F = 1 \rightarrow F'$ beam is reflected from a tip/tilt mirror below the cell. The $F = 2 \rightarrow F'$ beam is not retroreflected, and also serves as a probe beam for detection.

The MOT light is fiber coupled to the vacuum chamber via a three-way fiber beamsplitter and each beam is retroreflected. The MOT beams are 7 mm in diameter ($1/e^2$) and 6 mW of laser power is used per beam. Two of the MOT beams enter the cell at 45⁰. Typically, the cloud contains 10^7 atoms at the start of an interferometer sequence, and the initial Gaussian cloud diameter is ~500 μm (2 σ). The atom ball expands isotropically after release with a typical atom speed of about 3 cm/s ($T \cong 10\ \mu$K).
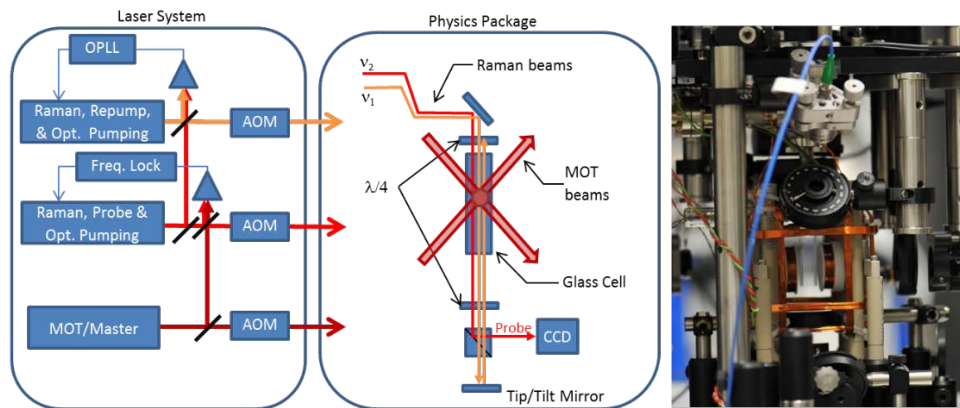
Figure 3. Schematic diagram of the laser system and physics package and an actual photo of the vacuum chamber surrounded by optics and coils. (Colour online).

4. Experiment

4.1. Typical Experimental Sequence

The main steps in a typical interferometer sequence are shown in Table I. The typical cycle time for one measurement is currently 3 s. This is limited by the camera read-out time and by the need to acquire background light and dark images for absorption detection, which does not allow for atom recapture. So far, we have not focused on minimizing the cycle time because we have been characterizing systematics and noise. In the near future, we will minimize the cycle time to optimize the instrument's sensitivity.

Table 1. Main steps in a typical interferometer sequence for observing interferometer fringes. For technical reasons, the acquisition of the light and dark images for absorption imaging is slow and not optimized in the experiment's current implementation. There are many other short trigger and wait periods needed to run the experiment that are not included in this list.

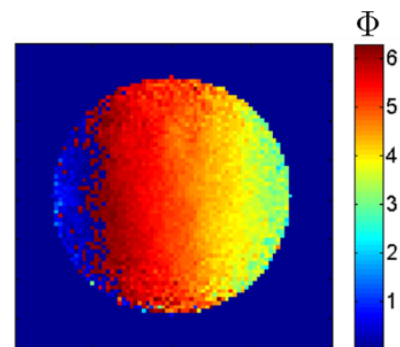| Time	Process
0 to 1.5 s	Load MOT
Next 5 ms	Optical Molasses
Next 1.4 ms	Steps to prepare atoms in $F = 1$, $m_F = 0$
Next 5 ms	Atoms undergo free fall and acquire velocity, which allows the Doppler sensitive and insensitive Raman transitions to be differentiated
Next 3 μs	First Raman $\pi/2$ pulse
Next 10 ms	Wait period T
Next 6 μs	Raman π pulse
Next 10 ms	Second wait period T
Next 3 μs	Second Raman $\pi/2$ pulse
Next 100 μs	Acquire absorption image of atoms in $F = 2$ state
Next 150 μs	Prep and pump $F = 1$ atoms into $F = 2$
Next 100 μs	Acquire absorption image of all atoms ($F = 1$ and $F = 2$)
Next 535 ms	Acquire light and dark reference images for $F = 1$ and $F = 1+2$ imaging conditions.

4.2. Simulating Rotations

We employ a commercial tip/tilt mirror as the Raman-beam retroreflecting optic to simulate and characterize rotations in our system. Compared to rotating the optical table, this approach is a simple way to simulate rotations that is equivalent to rotating the whole apparatus with respect to the local geostationary frame [16]. The mirror begins to rotate a few milliseconds before the first Raman pulse and rotates at a constant rate during the interferometer sequence.

4.3. Initial Results

We have demonstrated sensitivity to acceleration and rotation with our instrument. We have simulated two-axis rotations of the interferometer by tilting the Raman axis between light pulses. The spatial fringes have the expected properties; they are perpendicular to the axis of rotation, have a wavelength that is inversely proportional to the rotation rate Ω, and decrease in contrast with increasing Ω.

Figure 4. Spatial interference fringes from a rotation rate of $\Omega = 33$ mrad/s (S/N = 40). To construct this image, the Raman chirp rate was scanned over several interferometer fringes (100 images) and Φ was found from a sinusoidal fit to the atom population difference for each pixel. In an actual instrument, 3 images would be required to measure the phase map, and the S/N would be 7. Here, T was 6 ms. The image size is 1.75 mm ×1.75 mm. (Colour online).

5. Outlook

Our current efforts focus on measurements of the gyroscope's scale factor and dynamic range and related systematics. Our medium-term efforts will focus on understanding and reducing the noise, since the current signal-to-noise ratio for the interferometer fringes averaged over the cloud in our interferometer is only ~4. In the long term, we plan to characterize our interferometer as an inertial sensor and to explore the possibility of developing a truly miniaturized system.

References

[1] Hu Z-K, Sun B-L, Duan X-C, Zhou M-K, Chen L-L, Zhan S, Zhang Q-Z and Luo J 2013 Demonstration of an ultrahigh-sensitivity atom-interferometry absolute gravimeter, *Phys. Rev. A* **88** 043610

[2] Gustavson T L, Landragin A and Kasevich M A 2000 Rotation sensing with a dual atom-interferometer sagnac gyroscope, *Classical Quant Grav* **17** 2385-2398

[3] Durfee D S, Shaham Y K and Kasevich M A 2006 Long-term stability of an area-reversible atom-interferometer sagnac gyroscope, *Physical Review Letters* **97** 240801

[4] Berg P, Abend S, Tackmann G, Schubert C, Giese E, Schleich W P, Narducci F A, Ertmer W and Rasel E M 2015 Composite-light-pulse technique for high-precision atom interferometry, *Physical Review Letters* **114** 063002

[5] Jekeli C 2005 Navigation error analysis of atom interferometer inertial sensor, *NAVIGATION: Journal of The Institute of Navigation* **52** 1-14

[6] Stern G, Battelier B, Geiger R, Varoquaux G, Villing A, Moron F, Carraz O, Zahzam N, Bidel Y, Chaibi W, Pereira Dos Santos F, Bresson A, Landragin A and Bouyer P 2009 Light-pulse atom interferometry in microgravity, *The European Physical Journal D* **53** 353-357

[7] Geiger R, Menoret V, Stern G, Zahzam N, Cheinet P, Battelier B, Villing A, Moron F, Lours M, Bidel Y, Bresson A, Landragin A and Bouyer P 2011 Detecting inertial effects with airborne matter-wave interferometry, *Nat Commun* **2:474** doi: 10.1038 / ncomms1479

[8] Schmidt M, Senger A, Hauth M, Freier C, Schkolnik V and Peters A 2011 A mobile high-precision absolute gravimeter based on atom interferometry, *Gyroscopy and Navigation* **2** 170-177

[9] Kasevich M and Chu S 1991 Atomic interferometry using stimulated raman transitions, *Physical Review Letters* **67** 181-184

[10] Borde C J 1989 Atomic interferometry with internal state labelling, *Physics Letters A* **140** 10-12

[11] Canuel B, Leduc F, Holleville D, Gauguet A, Fils J, Virdis A, Clairon A, Dimarcq N, Bordé C, Landragin A and Bouyer P 2006 Six-axis inertial sensor using cold-atom interferometry, *Physical Review Letters* **97** 010402

[12] Müller T, Gilowski M, Zaiser M, Berg P, Schubert C, Wendrich T, Ertmer W and Rasel E M 2009 A compact dual atom interferometer gyroscope based on laser-cooled rubidium, *The European Physical Journal D* **53** 273-281

[13] Dickerson S M, Hogan J M, Sugarbaker A, Johnson D M S and Kasevich M A 2013 Multiaxis inertial sensing with long-time point source atom interferometry, *Physical Review Letters* **111** 083001

[14] Kasevich M, Weiss D S, Riis E, Moler K, Kasapi S and Chu S 1991 Atomic velocity selection using stimulated raman transitions, *Physical Review Letters* **66** 2297-2300

[15] Cheinet P, Pereira Dos Santos F, Petelski T, Le Gouët J, Kim J, Therkildsen K T, Clairon A and Landragin A 2006 Compact laser system for atom interferometry, *Applied Physics B* **84** 643-646

[16] Lan S-Y, Kuan P-C, Estey B, Haslinger P and Müller H 2012 Influence of the coriolis force in atom interferometry, *Physical Review Letters* **108** 090402